King Saud University

Arabian Journal of Chemistry

www.ksu.edu.sa
www.sciencedirect.com

ORIGINAL ARTICLE

Synthesis of activated carbon foams with high specific surface area using polyurethane elastomer templates for effective removal of methylene blue

Mahitha Udayakumar [a,b], **Bilal El Mrabate** [a,b], **Tamás Koós** [c], **Katalin Szemmelveisz** [c], **Ferenc Kristály** [d], **Máté Leskó** [d], **Ádám Filep** [a], **Róbert Géber** [e], **Mateusz Schabikowski** [f], **Péter Baumli** [g], **János Lakatos** [b], **Pál Tóth** [c], **Zoltán Németh** [a,*]

[a] *Advanced Materials and Intelligent Technologies Higher Education and Industrial Cooperation Centre, University of Miskolc, H-3515 Miskolc, Hungary*
[b] *Institute of Chemistry, University of Miskolc, H-3515 Miskolc, Hungary*
[c] *Department of Combustion Technology and Thermal Energy, University of Miskolc, H-3515 Miskolc, Hungary*
[d] *Institute of Mineralogy and Geology, University of Miskolc, H-3515 Miskolc, Hungary*
[e] *Institute of Ceramic and Polymer Engineering, University of Miskolc, H-3515 Miskolc, Hungary*
[f] *Institute of Nuclear Physics, Polish Academy of Sciences, PL 31-342 Krakow, Poland*
[g] *Institute of Physical Metallurgy, Metal Forming and Nanotechnology, University of Miskolc, H-3515 Miskolc, Hungary*

Abstract Carbon foams have gained significant attention due to their tuneable properties that enable a wide range of applications including catalysis, energy storage and wastewater treatment. Novel synthesis pathways enable novel applications via yielding complex, hierarchical material structure. In this work, activated carbon foams (ACFs) were produced from waste polyurethane elastomer templates using different synthesis pathways, including a novel one-step method. Uniquely, the produced foams exhibited complex structure and contained carbon microspheres. The ACFs were synthesized by impregnating the elastomers in an acidified sucrose solution followed by direct activation using CO_2 at 1000 ℃. Different pyrolysis and activation conditions were investigated. The ACFs were characterized by a high specific surface area (S_{BET}) of 2172 m^2/g and an enhanced pore volume of 1.08 cm^3/g. Computer tomography and morphological studies revealed an inhomogeneous porous structure and the presence of numerous carbon spheres of varying sizes

---

* Corresponding author.
  E-mail address: kemnemet@uni-miskolc.hu (Z. Németh).
Peer review under responsibility of King Saud University.

ELSEVIER | **Production and hosting by Elsevier**

embedded in the porous network of the three-dimensional carbon foam. X-ray diffraction (XRD) and Raman spectroscopy indicated that the obtained carbon foam was amorphous and of turbostratic structure. Moreover, the activation process enhanced the surface of the carbon foam, making it more hydrophilic via altering pore size distribution and introducing oxygen functional groups. In equilibrium, the adsorption of methylene blue on ACF followed the Langmuir isotherm model with a maximum adsorption capacity of 592 mg/g. Based on these results, the produced ACFs have potential applications as adsorbents, catalyst support and electrode material in energy storage systems.

1. Introduction

Carbon foams (CFs) are low density, porous materials that have gained significant attention over the past few decades due to their potential applications in various fields. Based on the applied pyrolysis temperature and type of precursor, CFs are classified as graphitic (Klett, 2019) and non-graphitic (Jana and Ganesan, 2009; Narasimman and Prabhakaran, 2012). Carbon foams are extensively used as electrode materials in energy storage systems (Amini et al., 2011; Zhou et al., 2017), as catalyst support (Qian et al., 2017; Wang et al., 2017), in heavy metal removal (Chen et al., 2013; Lee et al., 2015), CO_2 absorption (Liu et al., 2020; Narasimman et al., 2014; Rodríguez and García, 2017), electromagnetic shielding (Bychanok et al., 2015; Pastore et al., 2019), radionuclide trapping (Jana and Ganesan, 2009), and sound absorption (Gao et al., 2018; Letellier et al., 2017). The properties of CF depend largely on the temperature of heat treatment, the carbon precursor and other pyrolysis conditions. The specific pore structure makes CF lightweight with the adjustable surface, electrical, thermal and mechanical properties.

Several authors reported the synthesis of CF or reticulated vitreous carbon materials using fabrication techniques such as the blowing of carbon precursors, the template replica method, compression of exfoliated graphite, assembly of graphene nanosheets, etc. (Inagaki et al., 2015). Of these, the template carbonization method is the simplest and most efficient for obtaining CFs with tailored porosity and structure (Inagaki et al., 2015). This approach utilizes polyurethane (PU) foams, e.g., flexible foams (Qian et al., 2017; Saini et al., 2013) and rigid foams (Farhan et al., 2016), melamine or melamine–formaldehyde foams (Chen et al., 2013; Yu et al., 2018; Zhou et al., 2017), polystyrene foams (de Paula et al., 2018), poly(methyl methacrylate) (Lee et al., 2005), and zeolite foams (Saini et al., 2013) as templates. These templates are either directly carbonized at high temperatures in an inert atmosphere or they can be treated with a polymeric resin (a carbon source) for cross-linking before carbonization. Typical carbon sources used for this process are coal tar (Kumar et al., 2015), petroleum pitch (Yadav et al., 2011), phenolic resin (Lee et al., 2005; Nam et al., 2013; Qian et al., 2017), polyfurfural alcohol (Amini et al., 2011), polyimide (Inagaki et al., 2004) and sucrose (Jana et al., 2013; Saini et al., 2013).

Since the discovery of carbon nanotubes and fullerenes, great effort has been spent to synthesize carbon materials with various shapes and morphologies (e.g. fibres, onions, nanobuds, nanoribbons, etc). Among them, carbon spheres (CS) are gaining significant interest due to their versatile properties and wide-ranging applications. Carbon spheres can be used as electrodes in electrochemical systems such as batteries (Hu et al., 2020), supercapacitors (Du et al., 2020), fuel cells (Shu et al., 2018), as catalyst support (Tesfu-Zeru et al., 2017), sealants (Song et al., 2004), and in CO_2 capture (Li et al., 2020). Generally, carbon spheres are synthesized by one of two routes: i) high-temperature decomposition of materials containing carbon in an inert atmosphere through arc-discharge (He et al., 2007) followed by chemical vapour deposition (CVD) (Panickar et al., 2020) and laser ablation or plasma processes (Bystrzejewski et al., 2008; Yang et al., 2008); or ii) low-temperature pyrolysis and catalytic decomposition of organic compounds via e.g., the heat treatment of polymers or other materials, usually in an autoclave (Réti et al., 2017).

Porous carbon materials with a high specific surface area have attracted much interest, especially in the field of adsorption and catalysis. The morphology and size distribution of pores influence the specific surface area that is responsible for the surface activity. The surface properties of the carbon material can be easily altered by activation using a mild oxidizing agent. Previously, CFs prepared from different precursors were activated using physical (steam, CO_2) and chemical (KOH, NaOH, $ZnCl_2$) methods. The physical activation method is widely considered an efficient way to produce porous carbon materials since chemical activation requires highly corrosive agents and an additional washing step.

The pore structure is a critical factor influencing the adsorption capacity and rate capability of any carbon material (Mestre et al., 2009). The adsorption of small molecules such as CO_2 (molecular diameter of 0.33 nm) is determined by the distribution of ultramicropores, while the adsorption of large molecules such as Congo red (2.3 nm) and methylene blue (1.7 nm) happens in broadened pores (Li et al., 2018). Organic dyes and hydrated ions are best adsorbed in hierarchical pore structures.

In this work, a new pathway was developed for the synthesis of free-standing activated carbon foams (ACFs) containing CS evenly distributed in the foam. The synthesized material combines the advantages of CS such as increased surface, tuneable porosity and good packing density (Amorós-Pérez et al., 2018) with those of three-dimensional porous CF matrices. Polyurethane elastomeric foam (EF) was used as a base material and sucrose as a carbon source. The presented pathway appears feasible for the utilization of difficult-to-recycle, post-industrial polyurethane elastomer waste. To the authors' knowledge, no prior studies have synthesized CS-containing ACF using polyurethane elastomer templates. The synthesis process was extended with one-step activation using CO_2 that

resulted in CS-containing ACF with a high specific surface area. The activation process does not require expensive catalysts or complex purification. Finally, this work provides insight into the morphology and structural properties of ACFs produced from sucrose inside the pores of polyurethane elastomer templates. The adsorption performance of the ACFs was assessed by equilibrium studies of methylene blue (MB) dye adsorption. The foams have potential applications as catalyst supports or electrodes in energy storage devices.

2. Experimental section

In this section, details of the synthesis procedure and characterization methods are provided.

2.1. Materials

Polyurethane elastomers (post-industrial waste) were provided by Elastico Ltd. (Hungary). The concentrated sulfuric acid (96 wt%) and MB dye ($C_{16}H_{18}ClN_3S$) were purchased from VWR International Ltd., (Hungary). MilliQ water (18.2 MΩcm) and ordinary table sugar (sucrose from Magyar Cukor Zrt., Koronás ^{TM}, Kaposvár, Hungary) were used for the preparation of the carbon bead precursor solution. Carbon dioxide (purity > 99.995%) purchased from Messer Group GmbH (Germany) was used for the activation of CFs.

2.2. Preparation of activated carbon foams

The ACFs were prepared by using polyurethane elastomer as a sacrificial template. The templates were immersed in an acidified sucrose solution followed by carbonization and activation. The acidified sucrose solution and the carbon foams in N_2 atmosphere were prepared as reported previously (Udayakumar et al., 2019). In brief, the sucrose precursor solution was prepared by adding 40 ml of 2.8% (v/v) dilute sulfuric acid to 100 g of sucrose in a glass beaker followed by heating to 80 ℃ under continuous stirring until complete dissolution. The foams cut into 2.5 cm × 2.5 cm × 2.5 cm cubes were immersed and kept in the precursor solution for 12 h. The excess solution was removed from the samples by squeezing in paper tissues. Thereafter, the impregnated samples were dried overnight at room temperature. Dried samples were cross-linked in a hot air oven at 110 ℃ for 10 h. After impregnation and drying, the mass of the residual sucrose precursor that remained in the elastomers was approximately twice that of the original mass of the raw foam. For activation, two different approaches were investigated: a one-step and a two-step activation process.

2.2.1. Two-step activation
In the two-step process, the first step was the carbonization of impregnated polyurethane elastomers at 700 ℃ or 900 ℃ at a heating rate of 10 ℃/min in N_2 atmosphere (200 ml/min) for a dwell time of 60 min in a tube furnace (Carbolite® 1200 °C Split Tube furnace VST 12/900) (Udayakumar et al., 2019). In the second step, the carbonized samples were placed in a quartz crucible and activated inside a silica glass tube of the high-temperature tube furnace in a stream of CO_2 (200 ml/min). Then, the furnace was heated to a maximum temperature of 900 ℃ or 1000 ℃, with a heating rate of 10 ℃/min and the samples were left at this temperature for 100 min.

2.2.2. One-step activation
In the one-step, direct process, the impregnated polyurethane elastomer templates were directly activated using CO_2 gas without any prior carbonization. In this approach, the impregnated samples were activated in a stream of CO_2 with a flow rate of 200 ml/min and heated to 1000 ℃ at a heating rate of 10 ℃/min with varying times of activation (30, 50, 80, 100 and 130 min) to identify the best activation time. Black, highly porous ACF was obtained, as shown in Fig. 1.

For the rest of this paper, the CF prepared at 700 ℃ and 900 ℃ in N_2 are denoted as EF700 and EF900, respectively. Directly activated CF (one-step process) is denoted as EFAC1 and the foams activated after carbonization (two-step process) at 1000 ℃ in CO_2 for 100 min is labelled as EFAC2. Table 1 provides a summary of sample nomenclature. Fig. 2 shows a flowchart of the synthesis procedure.

2.3. Calculation of yield

The yield of each sample was calculated as:

Yield after carbonization, Y_C(%)

$$= \frac{\text{Mass after carbonization}}{\text{Mass after impregnation and drying}} * 100 \qquad (1)$$

Final Yield after activation, Y_A(%)

$$= \frac{\text{Mass after activation}}{\text{Mass after impregnation and drying}} * 100 \qquad (2)$$

2.4. Characterization

Thermogravimetric analysis (TGA) was carried out using a TG209 F3 Tarsus thermogravimetric analyser (NETZSCH-Gerätebau GmbH, Germany) to measure the thermal behaviour of the impregnated polyurethane elastomers in N_2 and CO_2 atmosphere. Furthermore, an approximate optimum

Fig. 1 Photograph of the ACF obtained using the one-step process (EFAC1).

Table 1 Sample nomenclature.

Label	Description
EF700	Pyrolyzed in N_2 at 700 ℃ for 60 min
EF900	Pyrolyzed in N_2 at 900 ℃ for 60 min
EFAC1 or EFAC1 (100 min)	Direct activation in CO_2 at 1000 ℃ for 100 min
EFAC2 or EFAC2 (1000℃)	First pyrolyzed in N_2 at 900 ℃ (60 min), then activated in CO_2 at 1000 ℃ for 100 min
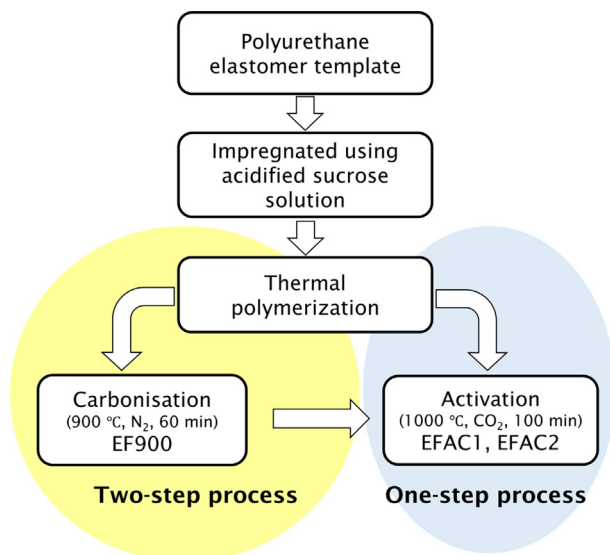
Fig. 2 Flowchart for the synthesis of activated carbon foams.

activation temperature was found using TGA. The elemental composition of ACFs was analysed using a Carlo Erba EA1108 CHNS-O analyser. Nitrogen adsorption–desorption experiments were carried out at 77 K to determine the Brunauer-Emmett-Teller (Brunauer et al., 1938) (BET) specific surface area (S_{BET}) using an ASAP 2020 instrument (Micromeritics Instrument Corp. USA). Before each measurement, the samples were degassed by holding at 90 °C for 24 h. The total pore volume was calculated from N_2 adsorption data at a relative pressure of 0.97. The micropore volume was obtained using the t-plot method. Mesopore volume was determined by the Barrett-Joyner-Halenda (BJH) method. The surface morphology of the carbon foams was investigated by Scanning Electron Microscopy (SEM) (Thermo Helios G4 PFIB Cxe) and the projections were made by Transmission Electron Microscopy (FEI Technai G^2-F20 HRTEM). The foam structure, pore size and particle size distribution of the CS were investigated using a YXLON FF35 dual-beam Computer Tomograph (CT). To determine the density of the CF, a Mohr-Westphal type density balance was used after plunging the specimens in ethanol. Averages of 5 independent measurements are reported (given in Table S1). The pore size distribution of the carbon foams and powdered samples (ACF crushed using mortar and pestle) were determined using mercury intrusion porosimetry (MIP). The tests were done using PASCAL 140 (low pressurization system down to 0.04 MPa) and PASCAL 440 (high pressurization system up to 400 MPa) instruments (Thermo Scientific). One test was performed on 3D

CF and 2 tests were run with powdered samples to cover the entire range of inter- and intraparticle pores present in the samples.

The structural properties of the CF were determined by the powder X-ray diffraction method (XRD) using a Bruker D8 Advance diffractometer with a Cu K-α radiation source (40 kV and 40 mA) in parallel beam geometry (Göbel mirror) with a position-sensitive detector (Vantec1, 1° opening). Measurements were taken in the 2–100° 2θ range with a goniometer speed of 0.007° 2θ/14 s. Samples were top-loaded on zero background Si sample holders. Raman spectroscopy measurements were carried out using a high-resolution Raman spectrometer (Nicolet Almega XR, Thermo Electron Corporation, Waltham, MA, USA) equipped with a 532 nm Nd:YAG laser (50 mW). Electrophoretic measurements were performed using a dynamic light scattering instrument (ZetaSizer NS - Malvern, UK). Wettability tests for all CF were carried out using the sessile drop method (SP 12 melt microscope - Sunplant Ltd., Hungary), via the acquisition of a silhouette shot. This method measures the angle of the sessile drop resting on the flat surface of the CF (polished using emery cloth sheets) using a goniometer – a microscope equipped with a video camera and a suitable magnifying lens, interfaced with a computer running image analysis software (KSV Instrument Ltd., Finland) to determine the tangent angle.

2.5. Adsorption test

For the equilibrium adsorption study, a stock solution (10 mmol/L) of MB was prepared and the desired concentrations (0.5, 1.0, 1.5, 2.0, 2.5, 3.0, 3.5 and 4.0 mmol/L) were obtained by subsequent dilution. The experiments were carried out using 8 Erlenmeyer flasks, each containing 0.1 g of powdered ACF (EFAC1 and EFAC2) and 50 ml of MB working solution (0.5–4.0 mmol/L). These flasks were shaken for 2 h at room temperature in a horizontal shaker. The adsorption of ACFs was tested with different contact times and equilibrium adsorption was achieved in 2 h. The parameters were selected based on preliminary studies such that full adsorption isotherms were obtained. After shaking, the mixtures were immediately centrifuged, the supernatant was collected and the residual MB concentrations were measured by a UV–Vis spectrophotometer (UV-6300PC Double Beam Spectrophotometer, VWR International Ltd.) at a maximum wavelength of 664 nm. The Langmuir and Freundlich isotherm models were used to describe the equilibrium characteristics of the adsorption of MB onto ACFs and the relevant equations (Eqs. S1-S3) are given in the Electronic Supplementary Material (ESM).

3. Results and discussion

The properties of the as-prepared CFs were tested using different characterization techniques and their results will be discussed in the sub-sections below:

3.1. Yield of carbon foams

Table 2 presents the experimental yields (using Eqs. (1) and (2)) of the ACFs obtained from the two different activation approaches and also the yields obtained from the TGA. In

Table 2 The calculated yield of the as-prepared ACFs.

Process	Sample	Mass of raw PU elastomer (g)	Mass after impregnation and drying (g)	Mass after carbonization (g)	Yield after carbonization (Y_C) (%)	Mass after activation (g)	Final yield after activation (Y_A) (%)
Experiment	EF900	0.5	1.6	0.4	25.0	–	–
	EFAC1	2.0	6.0	–	–	1.1	18.3
	EFAC2	3.5	10.5	2.6	24.8	1.4	13.3
TGA	EF900	–	–	–	30.8	–	–
	EFAC1	–	–	–	–	–	20.5
	EFAC2	–	–	–	30.8	–	14.5

both the process, the yield of the ACF prepared by the direct activation was higher than that obtained in the two-step process. The results of the TG analysis are explained in detail in the following Section 3.2.

3.2. Thermogravimetric analysis

The thermal behaviour of impregnated PU elastomers in the N_2 and CO_2 atmosphere at varying temperatures are shown in Fig. 3.

The thermograms in Fig. 3a and b represent the samples carbonized at 1100 ℃ at a heating rate of 10 ℃/min in N_2 and CO_2, respectively. The primary weight loss until 180 ℃ was due to the removal of residual water and the notable change at 180–320 ℃ was attributed to the pyrolysis or caramelization of acidified sucrose (Zhao et al., 2018) followed by the initiation of the urethane bond breakage. In the temperature range of 300–450 ℃, a sudden loss of mass was observed that might be due to the cleavage of hard and soft segments of urethane linkages leading to the formation of a primary amine, terminal alkene and CO_2, or the formation of a secondary amine and CO_2 (Nam et al., 2013). The remaining mass loss was due to the oxidation of carbon present in the sample with the evolution of CO and CO_2. The thermal behaviour of impregnated foams in N_2 (Fig. 3a) and CO_2 (Fig. 3b) was similar, with only a slight change in the mass loss beyond 1000 ℃ in the CO_2 atmosphere. Both gases behaved similarly, with the difference of N_2 acting as an inert gas even at high temperature, while CO_2 became more reactive at approximately 1000 ℃. Thus, the mass loss of 2.77% due to the removal of carbon in the form of CO and CO_2 can be observed in Fig. 3b. This was further investigated by heating the impregnated foams to 1000 ℃ in N_2 and CO_2 at a heating rate of 10 ℃/min with a dwell time of 60 min. Fig. 3c and d show that the total mass loss until 1000 ℃ was almost the same in N_2 and CO_2 atmospheres, respectively. However, the thermal behaviour at 1000 ℃ from the 100th to the 160th minute showed a significant difference between the environments. During this time, there was little mass loss in N_2 atmosphere (3.18%), whereas in CO_2 the mass loss was comparatively higher (10.43%). Therefore, it is clear that the critical temperature for the CO_2 gas to become more reactive was 1000 ℃ and the significant mass loss during the residence time revealed that the CO_2 gas removed increasingly more atoms from the carbon skeleton. Thus, CO_2 appeared to be a good activating agent for producing carbon foams with advantageous surface char-

acteristics. Furthermore, temperature and time play a crucial role in the activation process.

The two different activation approaches, i.e., the one-step and two-step processes, were compared based on the TG curves shown in Fig. 3d and Fig. 3e and f, respectively. Fig. 3d represents the one-step activation process, the mass loss behaviour of which has already been discussed. From this thermogram, the yield of the directly activated carbon foam was found to be 20.5% (residue). Fig. 3e and f represent the two-step activation process. The first step of carbonization was done in N_2 by heating at a rate of 10 ℃/min up to 900 ℃ with a dwell time of 60 min. The thermal behaviour was similar to that shown in Fig. 3c. In the second step, the produced char was activated in CO_2 at a heating rate of 10 ℃/min until 1000 ℃ with a dwell time of 60 min. In the two-step process, the yield of the obtained char in the first step was 30.8%. From the curve (Fig. 3f), the yield after the activation was calculated to be 14.5%. Thus, the yield obtained from the one-step process was higher than that of the two-step process. These results are in line with the experimentally determined yields with the CO_2 activation time of 100 min (Table 2).

3.3. Chemical analysis

The results of the chemical analysis of the as-prepared ACFs are given in Table 3.

Carbon contents of 97.0% and 94.8% were attained for CFs produced by the one-step and two-step activation process, respectively. These ACFs also contained traces of oxygen, hydrogen, nitrogen and sulfur. This residual content indicated the presence of surface functional groups. Supposedly, ACF prepared by the two-step process contained more material bound as surface functional groups than the foam synthesized by the one-step process, as it had higher carbon content. The samples did not contain any metallic impurities; the precursors were free from metal ions and no catalysts were used in the process.

3.4. Nitrogen adsorption test

Adsorption properties of the ACFs were determined by N_2 adsorption tests. The BET model was used for the estimation of surface area. For determining the micropore volume, the t-plot method was used. Table 4 summarizes the textural properties calculated from the obtained N_2 adsorption isotherm at 77 K. The pyrolysis of impregnated foams in N_2 (EF900)
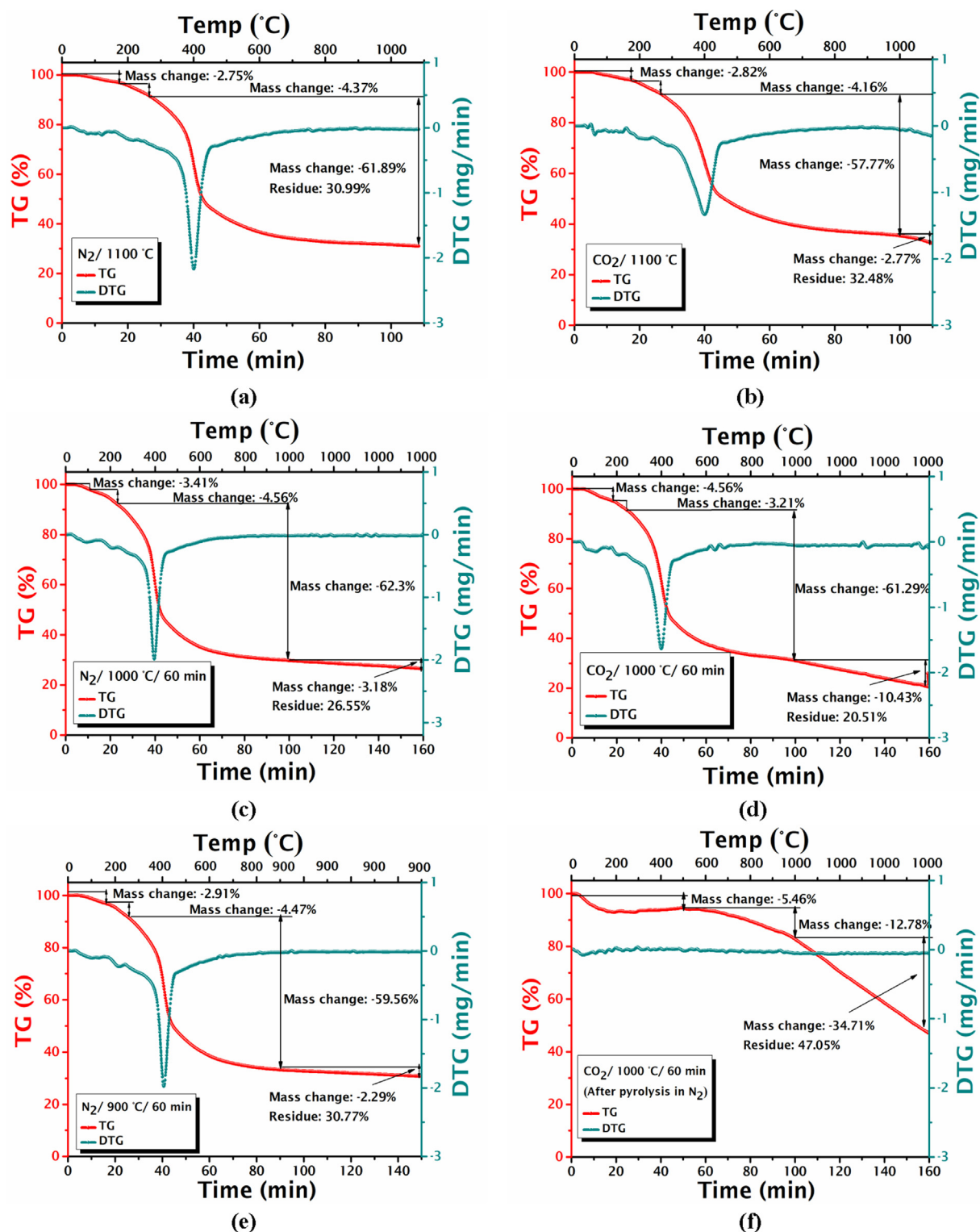
Fig. 3 TGA of the impregnated PU elastomer pyrolyzed in **(a)** N_2 at 1100 ℃; **(b)** CO_2 at 1100 ℃; **(c)** N_2 at 1000 ℃ for 60 min; **(d)** CO_2 at 1000 ℃ for 60 min (one-step process); **(e)** N_2 at 900 ℃ for 60 min (1st step of the two-step process); **(f)** CO_2 at 1000 ℃ for 60 min (2nd step of the two-step process).

exhibited a specific surface area of 370 m^2/g and a total pore volume of 0.21 cm^3/g, and these values were taken from our former study (Udayakumar et al., 2019). For this case, the nitrogen sorption isotherm represented the characteristic type I adsorption isotherm of the microporous structure. These micropores originated from the removal of surface O- and H- functional groups as tar and gas during pyrolysis. The textural properties of the char (EF900) were further enhanced by

Table 3 Chemical analysis of the ACFs.

Sample	C %(m/m)	H %(m/m)	N %(m/m)	S %(m/m)	O %(m/m)
EFAC1	97.0	0.12	0.92	0	1.96
EFAC2	94.8	0.28	0.91	0.03	3.98

Table 4 Textural properties of CFs.

Sample	Specific surface area (S_{BET})	Micropore area	External surface area	V_m [a]	V_{BJH} [b]	V_T [c]	V_m/V_T	Pore size
	(m^2/g)	(m^2/g)	(m^2/g)	(cm^3/g)	(cm^3/g)	(cm^3/g)	(%)	(nm)
EF900	370	338	32	0.18	0.018	0.21	85.7	2.2
EFAC2 (900 ℃)	328	285	43	0.18	0.027	0.22	81.8	2.7
EFAC2 (1000 ℃)	633	522	111	0.33	0.066	0.41	80.5	2.6
EFAC1 (30 min)	334	290	44	0.13	0.017	0.16	81.3	1.92
EFAC1 (50 min)	896	762	134	0.36	0.034	0.43	83.7	1.90
EFAC1 (80 min)	1058	765	293	0.35	0.067	0.50	70.0	1.89
EFAC1 (100 min)	2172	577	1595	0.24	0.452	1.08	22.2	2.0
EFAC1 (130 min)	1421	561	860	0.25	0.255	0.71	35.2	1.99

[a] Micropore volume determined using t-plot; [b] BJH adsorption cumulative pore volume of pores between 1.7 nm and 300 nm; [c] Total pore volume at $P/P_0 \sim 0.97$.

CO_2 activation. The more suitable temperature for activation was found to be 1000 ℃, as the specific surface area decreased upon activation at 900 ℃ (328 m^2/g). This might be due to the less reactive nature of CO_2 at 900 ℃. Thus, the maximum specific surface area of CF obtained by two-step activation was 633 m^2/g – this corresponded to activation at 1000 ℃ for a dwell time of 100 min.

The highest specific surface area, 2172 m^2/g, and a total pore volume of 1.08 cm^3/g were obtained with direct, one-step activation at 1000 ℃ in a stream of CO_2 for 100 min. In both approaches, some of the carbon in the matrix was gasified, leading to the generation of new micropores with subsequent pore widening. Simultaneously, the release of CO and CO_2 further increased porosity.

The thermal decomposition of impregnated foams in N_2 or CO_2 led to the release of volatile matter in the form of vapours, tars and gases with the creation of pores in the residual char. The primary constituents of tar are aromatic hydrocarbons: toluene, furan, phenol and polycyclic aromatic hydrocarbons (PAHs) (Ukanwa et al., 2019). The primary tars can undergo polymerization reactions and secondary char formation as proposed by Gilbert et al. (Gilbert et al., 2009). In one-step activation at 1000℃ for 100 min, the CO_2 that reacted with tars released from impregnated foams, hindering the polymerization reaction and secondary char formation, resulted in high specific surface area. However, in the two-step process, the formation of these condensable tars during pyrolysis in N_2 created secondary char, completely or partially filling the created pores, resulting in chars with a lower surface area (633 m^2/g). During the activation of this char at the same condition as with direct activation (1000 ℃ for 100 min), the CO_2 removed the condensed tar particles from the pores and created new micropores, as indicated by high micropore surface area (522 m^2/g) and increased micropore volume (0.33 cm^3/g). Due to the secondary char formation, the surface area of the ACF produced in the two-step process was lower than that of the direct-activated ACF at the same condition.

According to the International Union of Pure and Applied Chemistry (IUPAC), adsorbent pores are classified as micropores (< 2 nm), mesopores (2–50 nm) and macropores (> 50 nm) (Sing et al., 1985). In one-step activation, the proportion of micropores progressively increases with an increase in the activation time. Once the activation time is increased beyond 100 min, the proportion of meso- and macropores sharply increases with a considerable drop in the proportion of micropores. Direct activation also increased the total pore volume of the samples, especially at longer activation times. Thus, the activation time is another critical parameter for optimizing porosity. The proportion of micropore, mesopore and macropore volume to the total pore volume was calculated for each sample and depicted in Fig. 4a. The lower proportion of micropore volume to the total pore volume of EFAC1 (100 min), 22.2%, and increased external surface area (1595 m^2/g) indicated the formation of many mesopores interconnected with continuous macropores. Meso- and macropores are transport pores that influence the adsorption kinetics and diffusion rate of the adsorbate within the material. The pore volume between the pore size of 1.7 and 300 nm was approximately 42% of the total pore volume; this has substantially increased in the case of EFAC1 (100 min).

The adsorption–desorption isotherms of the activated carbon foams are shown in Fig. 4b. All samples exhibited a typical type I adsorption isotherm of the microporous structure. Although the isotherm of EFAC1 (100 min) was still classified as type I, the increased volume of adsorbed N_2 and a narrow hysteresis (shown in Fig. 4b) associated with capillary condensation in mesopore structures, corresponding to a combination of type I and type IV isotherms, representing a micro-mesoporous structure (Cychosz et al., 2017). Moreover, the increase of the volume of adsorbed N_2 indicates a larger surface area and enhanced pore volume due to the extension of micropores and creation of new mesopores and macropores, indicating the potential for applications as an adsorbent with a hierarchical pore configuration. Table 5 provides a compar-
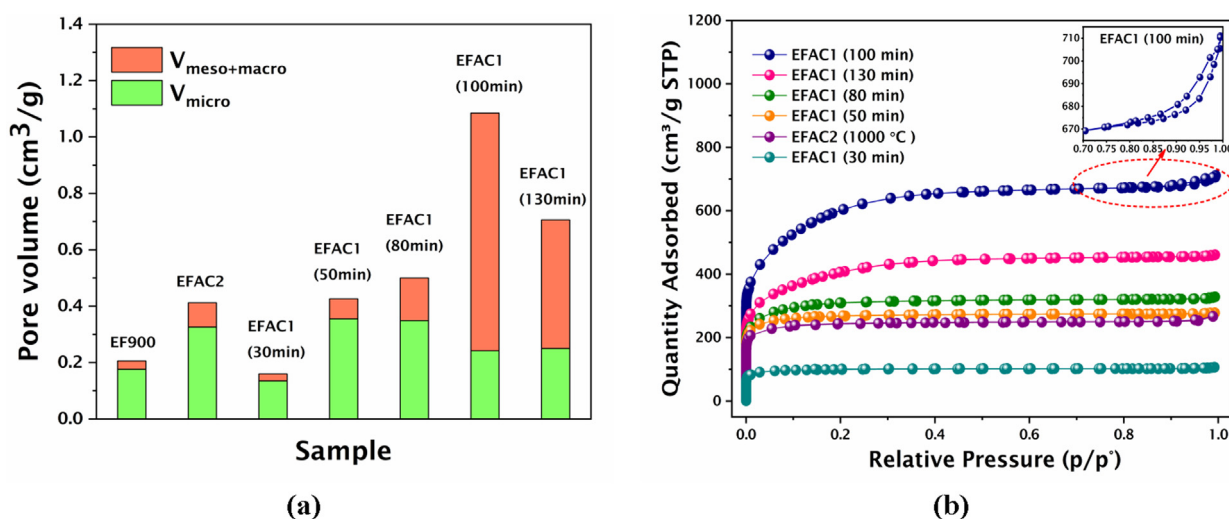
Fig. 4 **(a)** Pore volume distribution of carbon foams with various pore size ranges; **(b)** N_2 adsorption–desorption isotherms of the ACFs. The hysteresis of EFAC1 (100 min) is shown as an inset.

Table 5 Comparison of S_{BET} values of the current work with previously reported values.

Precursor	Process	Activating agent	S_{BET} (m^2/g)	Ref.
Polyurethane elastomer - sucrose	Direct activation	CO_2	2172	Current work
Melamine sponge	Carbonization followed by chemical activation	KOH	1136	(Cao et al., 2020)
Pinus nigra pine	Carbonization followed by chemical activation	KOH	76.9 ± 2.8	(Khalid et al., 2020)
Buckwheat flour	Direct activation	KOH	1555	(Huang et al., 2019)
Glucose	Hydrothermal synthesis followed by direct activation	KOH	3106.7	(Li et al., 2016)
Phenolic resin	Carbonization followed by physical activation	Steam	727.62	(Zhao et al., 2009)
Spruce tree sawdust	Carbonization followed by activation	KOH	716	(Yargic and Ozbay, 2019)
Coal tar pitch	Carbonization followed by physical activation	Steam	933	(Tsyntsarski et al., 2012)
Mimosa tannin extract	Carbonization followed by chemical activation	$ZnCl_2$, H_3PO_4	1265, 1875	(Tondi et al., 2010)
Furfural alcohol	Direct activation	$ZnCl_2$	652	(Cepollaro et al., 2020)

ison of the S_{BET} of the carbon foam synthesized in this study with that of similar, previously reported materials.

3.5. Pore size distribution

To better characterize the macroporosity of the samples, mercury intrusion porosimetry was used. The meso- and macropore size distributions of the CFs and their powdered samples were determined in the range of 4 nm to 110,000 nm. Plotting the cumulative pore volume (CPV) against the pore diameter (Fig. 5) shows a continuous increase in the mercury uptake with a decrease in the pore diameter. The pore size distribution of the 3D CFs was analysed, as it is relevant for their application as a support material. The comminution of the 3D EFAC1 shifted the peaks towards the smaller pore size ranges and the number of pores below 100 nm increased. The pore volume and size distribution of EFAC1 in powder form displayed a multimodal distribution with four intrusion steps in the domain of meso- and macropores from 4.7 nm to 17 μm, as shown in Fig. 5b. In both forms, EFAC2 exhibited a wider

pore size distribution with four intrusion steps; the respective pore sizes are marked in Fig. 5c and 5d. Results from MIP and N_2 adsorption analysis corroborate the hierarchical pore structure of the synthesized ACFs.

3.6. Morphological investigation

SEM micrographs of carbonized and activated CFs are shown in Fig. 6. The higher magnification micrographs of EF900 and EFAC2 showed a disordered microstructure with pores and interconnected threads of varying morphology as shown in Fig. 6b, f. However, the morphology of EFAC1 was nearly homogeneous with uniform pores and threads (Fig. 6d). Moreover, numerous spherical structures were seen on the walls, threads and porous bed of the CFs. The spheres were clearly identified in TEM micrographs.

The TEM micrographs (Fig. 7) of the carbonized and activated CFs display the presence of spherical carbon particles with varying sizes between 10 and 400 nm. Web-like arrangements of amorphous carbon particles around the carbon
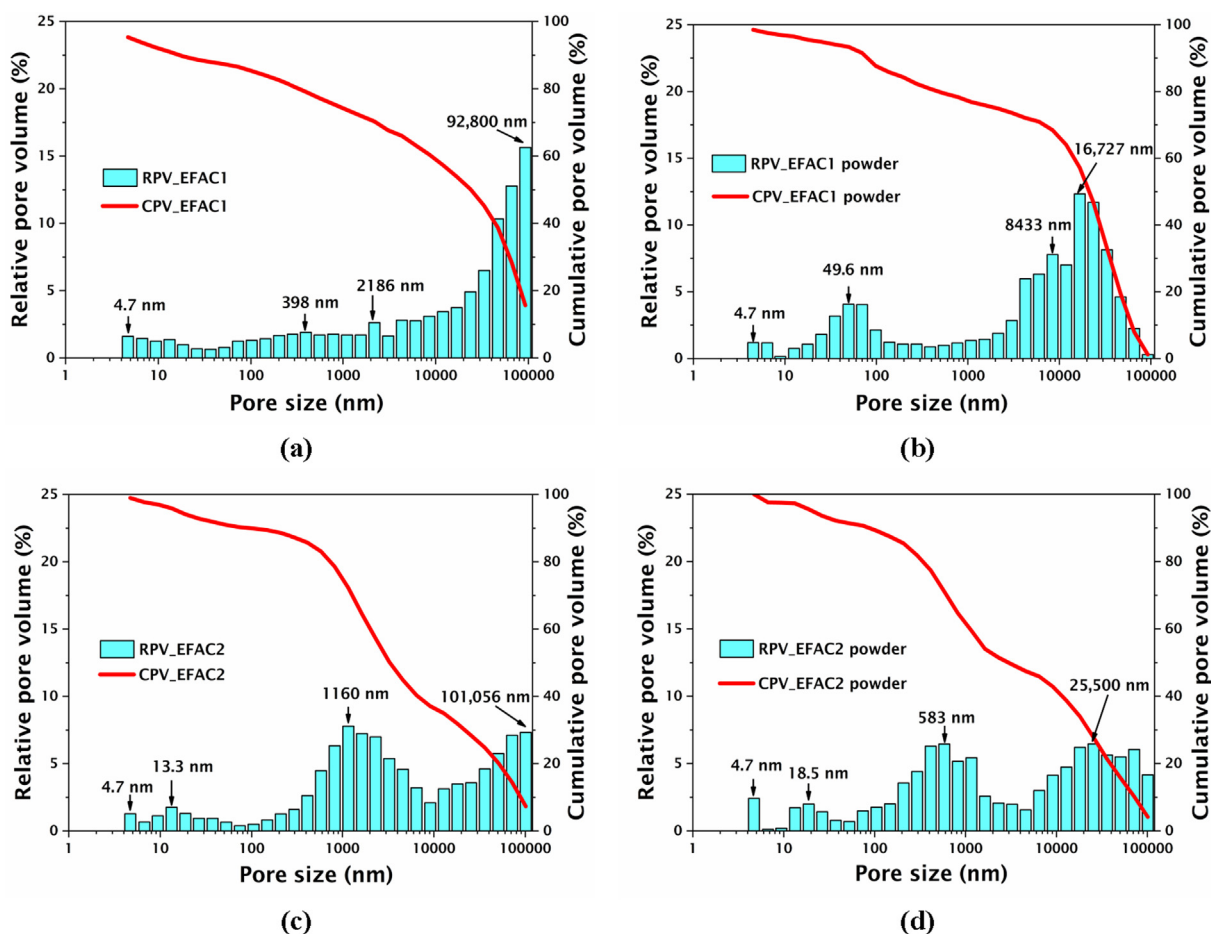
Fig. 5 MIP pore size distribution of 3D CFs **(a)** EFAC1; **(c)** EFAC2 and powdered samples **(b)** EFAC1; **(d)** EFAC2.

spheres of EFAC1 (Fig. 7b) and most pores appeared mesoporous, which again confirmed the higher porosity and specific surface area of EFAC1. These carbon particles are dense and perfectly spherical in shape.

Generally, spherical carbon particles provide better packing density than non-spherical structures (Cao et al., 2021). A promising future research direction is the application of the as-prepared carbon material as electrodes in supercapacitors. Electrodes fabricated from carbon foams containing carbon spheres with dense structure have the advantage of high packing density compared to other forms of amorphous carbon. The high packing density of active materials is desirable for achieving high volumetric capacitance, energy and power densities (Lee et al., 2016). Usually, 3D porous carbon has low packing density due to a large void fraction, leading to low volumetric capacitance (Cao et al., 2021). On the other hand, they provide high gravimetric capacitance due to their large accessible specific surface area. Thus, the porous ACF containing carbon spheres provides a compact structure while retaining high porosity that might be advantageous for attaining high volumetric and gravimetric capacitance.

3.7. Computer tomography analysis

Three-dimensional CT images of the raw PU elastomer and CFs are shown in Fig. 8.

Many spherical and cylindrical pores could be observed inside the pure polyurethane elastomer (Fig. 8a and Video S1 in the ESM). This porous architecture could act as a template for the formation of carbon spheres inside the foam structure. As polymeric materials have a high carbon content and a unique π-conjugated system, the pyrolysis of polymers leads to the formation of nanotubes, nanospheres, etc. (Deshmukh et al., 2010). Besides, sucrose can be widely used as a carbon source for the synthesis of carbon spheres, mainly in autoclave processes (Réti et al., 2017). Therefore, potentially, both the polymer template and the sucrose precursor played a significant role in the formation of carbon spheres. The formation of carbon spheres inside the foam can be explained with reference to the mechanism proposed by Zheng et al. (Zheng et al., 2009): the diluted sulfuric acid hydrolyzed the glycosidic bonds of sucrose and formed glucose and fructose monomer units. Further dehydration occurred upon drying at a low temperature (110 ℃) and during pyrolysis or activation in the tube furnace at a temperature between 160 and 200 ℃, polymerization took place to form colloidal carbon spheres inside the porous polyurethane elastomer template. When the temperature reached 300–400 ℃, the colloidal carbon spheres were subjected to self-assembly and aggregation. At higher temperatures (above 450 ℃), the spherical aggregates were fused into solid carbon spheres of varying sizes. With the evidence of the pore and particle size distribution of the CFs
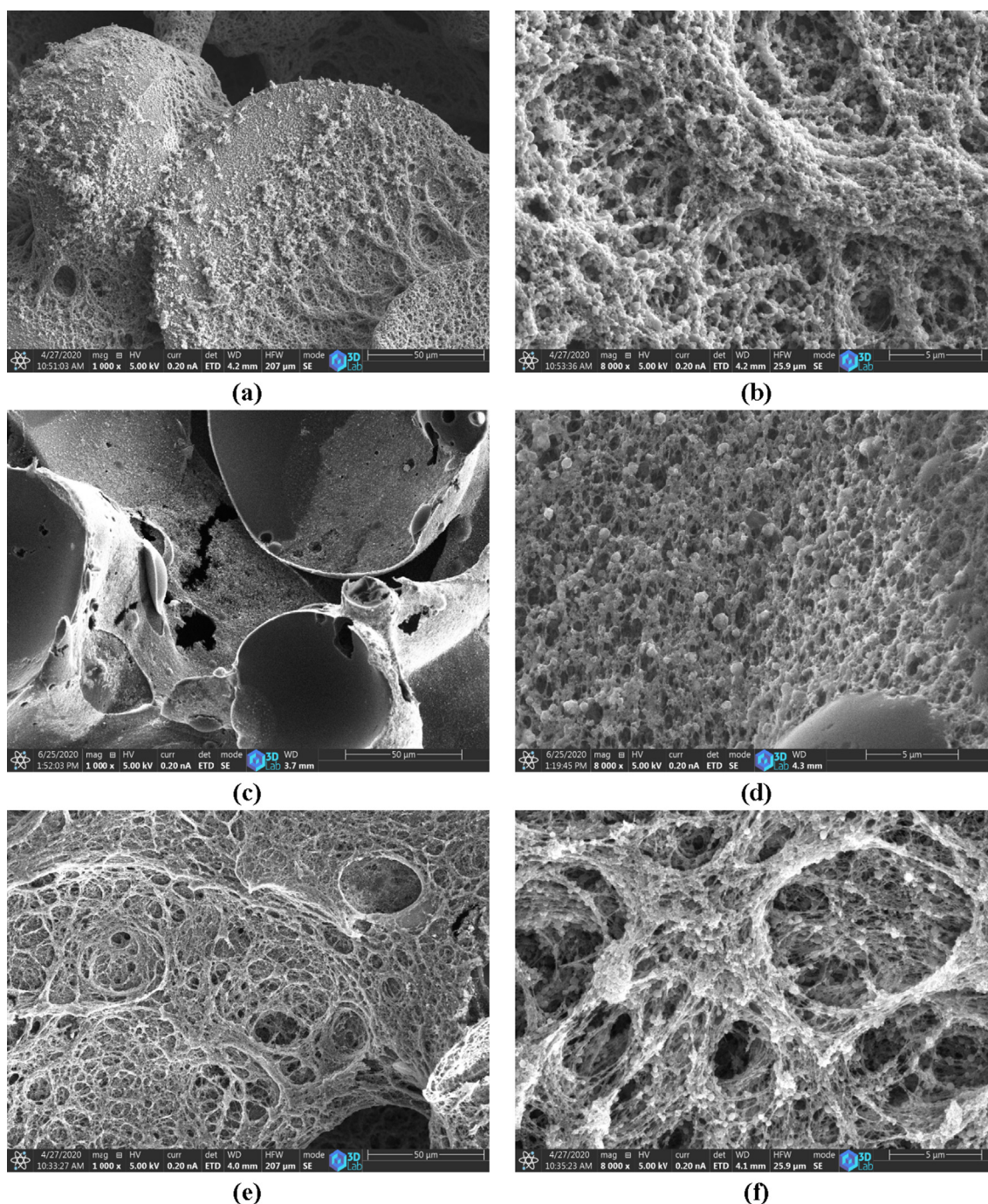
Fig. 6   SEM micrographs of **(a, b)** EF900; **(c, d)** EFAC1; **(e, f)** EFAC2.

calculated from CT imaging, it appears likely that during pyrolysis and activation, the carbon spheres were formed from the sucrose precursor filled inside the spherical pores of the polymer template, as seen in Fig. 8b-d and Video S2 in the ESM. The macropores or interconnected channels of the carbon foams were also visible in the CT images (Fig. 8b-d). The pore and particle size distribution of the raw PU elastomer and CFs are shown in Fig. 9.

As seen in Fig. 9a, the sizes of major pores of the polyurethane template were in the range of 50–300 μm. Similarly, the particle sizes of carbon spheres were between 50 and 200 μm (in Fig. 9b-d). Thus, it appears that the pore size distribution of the polyurethane template was a factor that influenced the size of carbon spheres. Note that the CT analysis only provided the pore and particle size distribution in the micrometre range.

3.8. XRD and Raman analysis

The structural properties and the type of carbon obtained were investigated by XRD and Raman spectroscopy (shown in

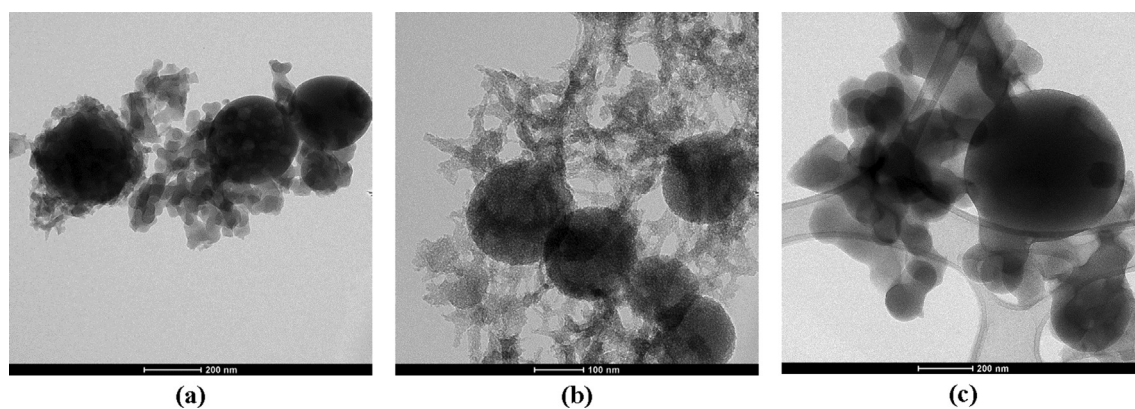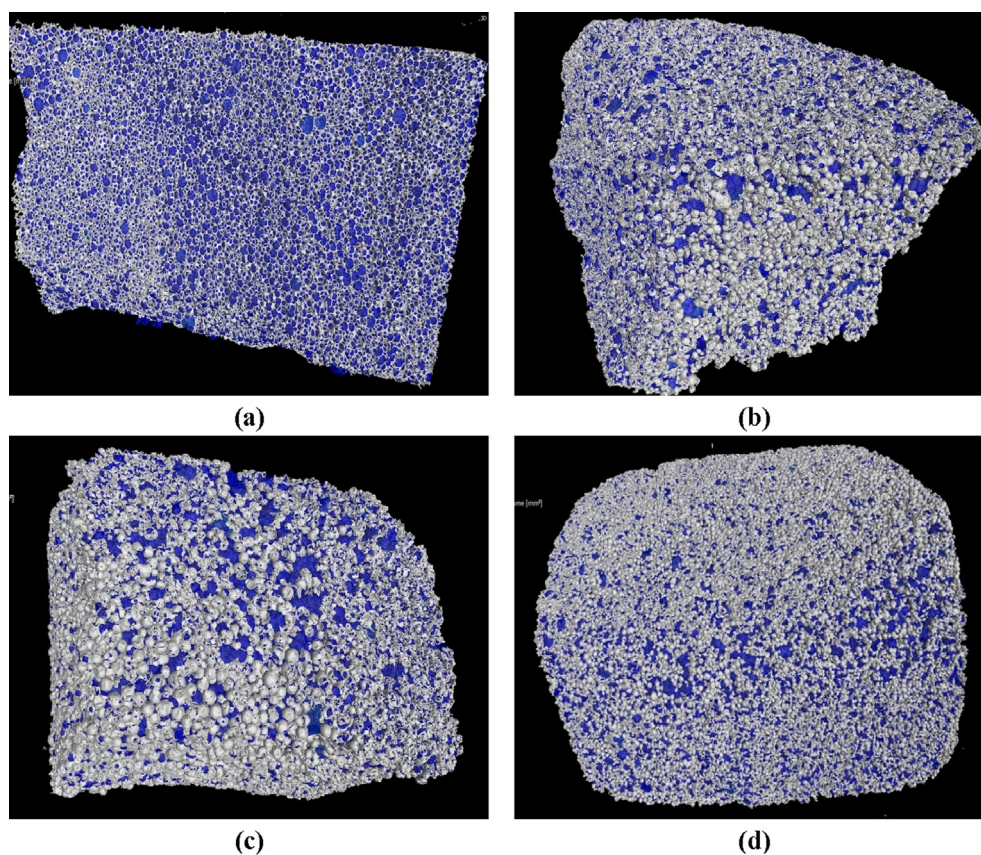**Fig. 7**   TEM micrographs of **(a)** EF900; **(b)** EFAC1; **(c)** EFAC2.

Fig. 8   CT images of **(a)** raw polyurethane elastomer; **(b)** EF700; **(c)** EF900; **(d)** EFAC1. The blue colour represents the pores and the white particles in (b) - (d) are the carbon spheres.

Fig. 10). Fig. 10a shows the XRD diffractogram of CFs with (EFAC) and without activation (EF700 & EF900). The diffractograms exhibited two broadened and weak diffraction peaks at $21.5° ≤ 2θ ≤ 23.5°$ and around $43.5°$ that correspond to the respective (0 0 2) and (1 0 0) diffraction of the amorphous or disordered turbostratic carbon skeleton (Hao et al., 2017; Nam et al., 2013). These peaks are of low intensity and not well-defined. This indicates a low degree of graphitization of the obtained carbon irrespective of the activation process. Therefore, from the XRD investigation, it can be observed that the obtained CFs were of a non-graphitized, turbostratic structure, in line with earlier results (Nam et al., 2013).

Raman spectra of the CF prepared at temperatures 700, 900 and 1500 ℃ in N_2 atmosphere and the ACF are shown in Fig. 10b. The spectrum "EF1500" represents the CF prepared at 1500 ℃ in N_2 and was included to provide a reference to compare with the Raman spectra of the samples prepared at lower temperatures. The first-order region in the Raman spectra displayed two main peaks at around 1340 cm^{-1} and 1580 cm^{-1}. The former peak is usually referred to as the D-band (or defect-induced band), attributed to the vibration of carbon atoms with dangling bonds in planar termination of the disordered graphite-like framework (Torad et al., 2014) and the latter peak is the G-band (graphitic band), correspond-
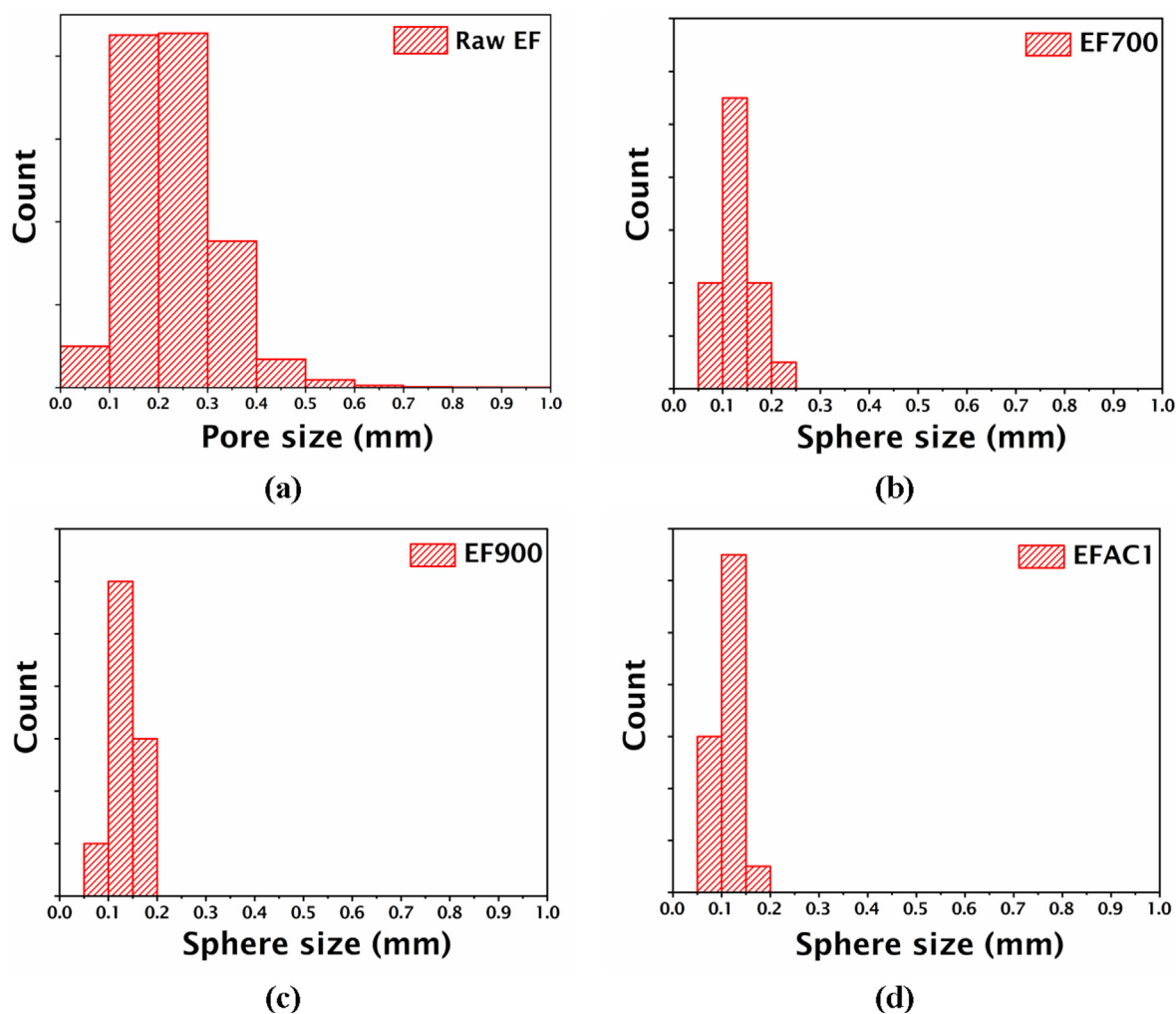
Fig. 9 Pore size distribution calculated from CT images of **(a)** raw PU elastomer; particle size distribution of **(b)** EF700; **(c)** EF900; **(d)** EFAC1.
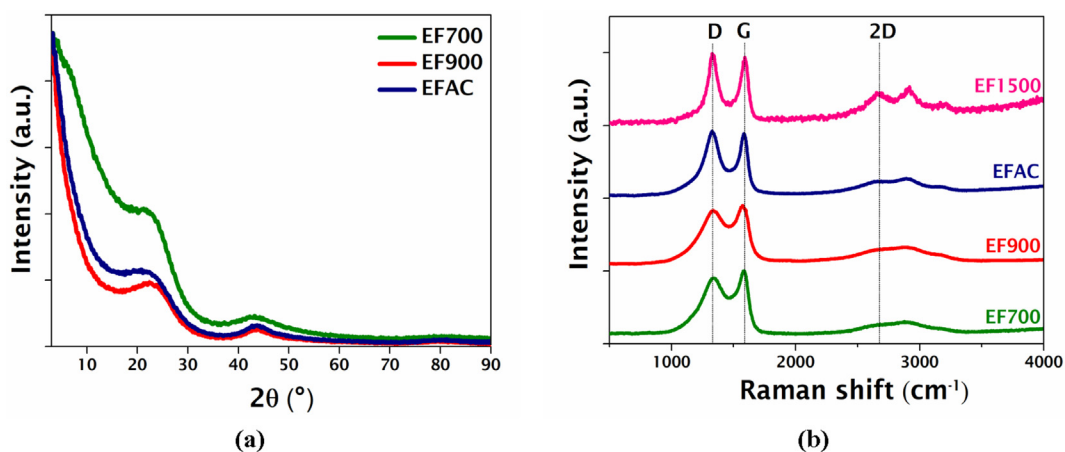

Fig. 10 **(a)** Powder XRD and **(b)** Raman spectra of carbonized (EF700, EF900, EF1500) and activated CF (EFAC). Activated samples (EFAC1 and EFAC2) displayed similar XRD and Raman spectra; therefore, here it is referred to as 'EFAC'.

ing to the in-plane stretching motion of sp^2-bonded carbon atoms with E_{2g} symmetry (Sze et al., 2001). The band observed around 2695 cm^{-1} as a rising peak in the spectrum of EF1500

and a broad modulated bump of the three Raman bands (in EF700, EF900, EFAC) is the overtone of the first order bands usually referred to as G□ or 2D peak. Generally, the ratio of

intensities of D and G bands (I_D/I_G) provides information about the size and structural network of the graphite crystals. The relative peak intensity of D and G peaks are given in Table S2. Another band (D $\square$ peak) appeared around 1600 cm^{-1} that merged with the G band in all four samples, are similar to very small and disordered crystals with little three-dimensional order as reported previously (McCulloch et al., 1994). Furthermore, while considering the bandwidth (full width at half maximum, FWHM) of the peaks D and G, usually the ordered crystals acquire γ_D and γ_G values in the range of 60–65 cm^{-1} and 25–50 cm^{-1}, respectively (Escribano et al., 2001). Here, the γ_D value of EF700 and EF900 was approximately 270 cm^{-1}, representing a disordered carbon structure and the values decreased to approximately 190 cm^{-1} and 100 cm^{-1} for the samples EFAC and EF1500, respectively. Thus, the decreasing bandwidth of the D peak for the activated and carbonized foams at high temperature indicates the ordering of the graphitic crystallite domains in the sample. Moreover, the merging of the G and D $\square$ peak increases the width of the G peak with the γ_G value around 110 cm^{-1} for EF700 and EF900, 93 cm^{-1} for the activated sample (EFAC) and 75 cm^{-1} for the sample carbonized at high temperature (EF1500). These values further indicate that the CF possessed a structure with little in-plane graphitic order and negligible three-dimensional ordering. Besides, the broad and low intensity of the 2D peak indicates an irregular or disordered arrangement of the graphitic framework.

The reason for the existence of the D peak is still not clear. According to Tuinstra and Koenig (Tuinstra and Koenig, 1970), the ratio of the peak intensity of D and G bands is inversely proportional to the size of the graphitic crystallites present in the sample i.e. $I_D/I_G = C/L_a$, where C = 4.4 nm for an excitation wavelength of 515.5 nm and L_a is the size of the crystallite. Later, Ferrari and Robertson (Ferrari and Robertson, 2000) reported that the T-K rule was no longer valid for amorphous carbon since increasing defects and reducing L_a below 2.5 nm, the decreased number of ordered rings are indicated by a smaller D-band ($I_D/I_G \propto L_a^2$), therefore the D-band and the intensity ratio (I_D/I_G) decreases with increasing amorphization. This fact was further confirmed by Jurkiewicz et al. (Jurkiewicz et al., 2018) while investigating the structure of glassy carbon produced at temperatures below 1000 °C. Thus, the shorter D-band and the decreased intensity ratio of the CF prepared at low temperatures (EF700, EF900) represented the disordered sp^2 bonded carbon with distorted pentagonal, hexagonal folded rings or rings of other orders. At higher temperatures (EFAC and EF1500), the development of the D-band and increased intensity ratio indicated the ordering of hexagonal carbon network or graphene layers to a certain extent. Thus, both the carbonized and activated CF had a turbostratic structure with small or disordered crystals with little or no three-dimensional ordering.
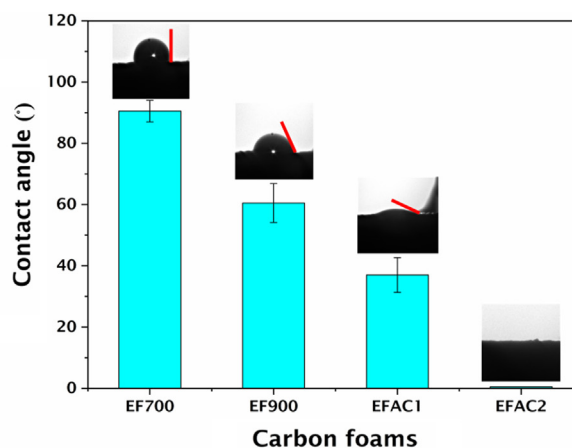
3.9. Zeta potential and wettability

Fig. 11a shows the zeta potential of powdered carbon foams in solutions of different pH. The pH-dependent surface charge provided insight into the surface functional groups of the CF. The pH at which the zeta potential equals zero is called the isoelectric point (pH$_{iep}$). The zeta potential of carbonized (EF900) and activated CF (EFAC1 & EFAC2) declined from + 12 mV to −24 mV, +21 mV to −23 mV, and + 21 mV to −22 mV, respectively, when the pH of the solution was increased from 3 to 9. It can also be observed that all three samples displayed zeta potential values of approximately −20 mV at pH 7.0. Extrapolation to the pH-axis yielded an estimate of pH$_{iep}$ of 3.7 for the carbonized (EF900) and 4.5 and 4.0 for the activated samples EFAC1 and EFAC2, respectively. The activation process shifted the pH$_{iep}$ towards higher values and it was apparent that the activation by CO_2 increased the surface basicity of the samples.

Contact angles measured using a polar liquid (deionized water) were found to be dependent on the pyrolysis and/or activation process as shown in Fig. 11b. The reported angles measured were based on the Circle and Young-Laplace methods (Carrier and Bonn, 2015) and their results are shown in Table S3. A significant decrease in the contact angle was observed for the activated CFs (EFAC1 & EFAC2). The ACF prepared by the two-step process were superhydrophilic due to their specific porosity and surface
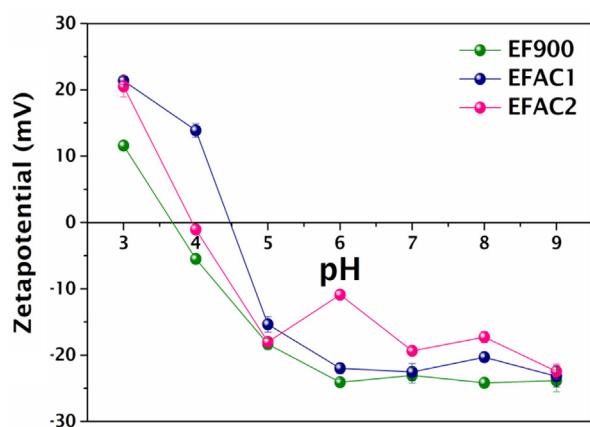
(a)

(b)

Fig. 11 **(a)** Zeta potential of carbonized (EF900) and activated CFs (EFAC1, EFAC2) at varying pH; **(b)** Wettability of carbonized (EF700, EF900) and activated CFs (EFAC1, EFAC2).

functional groups introduced during the CO_2 activation. Carbon-oxygen was the most important surface groups that influenced the surface characteristics, i.e., wettability of the material. Here, activation increased the pH_{iep} to 4 and 4.5, possibly due to the presence of basic surface functional groups that could improve the hydrophilicity of the material. Thus, the decrease of the contact angle (increasing hydrophilicity) could be attributed to the activation by CO_2, since it modified the carbon surface via the introduction of oxygen surface functional groups.

3.10. Equilibrium adsorption study

The adsorption isotherms allowed for evaluation of the nature of the adsorption process of MB on ACFs. The adsorption iso-

therms of MB on ACF plotted with the linearized Langmuir and Freundlich models are shown in Fig. S1. The comparison of the correlation coefficient (R^2) of the linear fits suggests that the Langmuir model (Fig S1a & b) yielded a better fit ($R^2 = 0.9998$) for the experimental equilibrium adsorption data than the Freundlich model. This indicates that the adsorbed MB formed a monolayer on the activated carbon surface and adsorption sites possessed uniform adsorption energies (Chen et al., 2016). Fig. 12a & b represent the MB adsorption isotherms (non-linear fits of the Langmuir and Freundlich equations) of the ACFs and the coefficients of the Langmuir and Freundlich models are given in Table 6. The maximum adsorption capacity of EFAC1 and EFAC2 was calculated from the non-linear Langmuir equation as 592 mg/g and 437 mg/g, respectively. The separation factor indicated
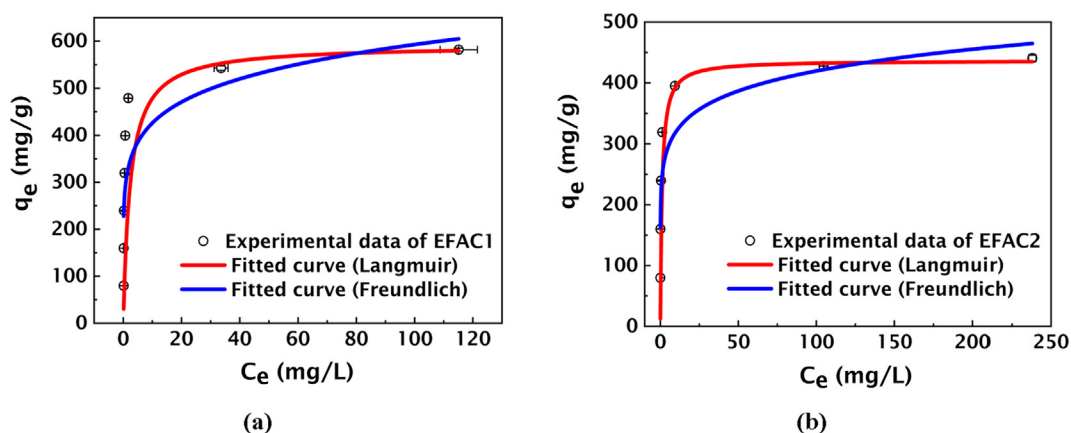

Fig. 12 Langmuir isotherms for the adsorption of MB on **(a)** EFAC1 and **(b)** EFAC2. In this figure, q_e is the amount of MB adsorbed at equilibrium (mg/g); C_e is the equilibrium concentration of MB (mg/L)

Table 6 Isotherm parameters for the adsorption of MB on ACFs.

	Langmuir model			Freundlich model	
	q_m (mg/g)	K_L (L/mg)	R_L range	K_F (mg/g)	n (L/mg)
EFAC1	592	0.42	0.001 – 0.015	281.6	4.78
EFAC2	437	0.92	0.0008 – 0.0067	223.8	6.08

The coefficients of Langmuir and Freundlich isotherm were calculated using non-linear regression (Orthogonal Distance Regression Iteration method).

Table 7 Adsorption capacities of MB of various previously reported adsorbents and the as-prepared CF.

Adsorbent	Precursor	Activating agent	S_{BET} (m^2/g)	q_m (mg/g)	References
Carbon foams	Polyurethane elastomer - sucrose	CO_2	2172; 633	592; 437	Current work
	Sucrose	Steam	601	85	(Varila et al., 2019)
	Spruce bark extracts	$ZnCl_2$	1495	240	(Varila et al., 2020)
	PU foam – activated carbon	Only carbonization	655	100	(Li and Liu, 2012)
Other activated carbon	Coconut shell	NaOH	876	200	(Delle Site, 2001)
	Commercial sucrose	KOH	1534	704	(Bedin et al., 2016)
	Fishery waste	NaOH	1868	185	(Marrakchi et al., 2017)
	Waste black tea	H_3PO_4	2054	402	(Borah et al., 2015)
	Date press cake	KOH	2633	547	(Heidarinejad et al., 2018)
	Sucrose	CO_2	1012	211	(Bedin et al., 2018)

strong interaction between the MB and the ACF adsorbent and showed that adsorption was favourable ($0 < R_L < 1$).

The high surface area EFAC1 (2172 m^2/g) resulted in the highest q_m, while the highest affinity (K_L) towards MB was observed in the case of EFAC2. Some of the micropores in the adsorbent were too small for the diffusion of MB molecules (1.7 nm); however, larger micropores and mesopores could easily adsorb MB molecules, increasing adsorption capacity. Both adsorbents showed good adsorption capacity due to their hierarchical pore structure, especially in the case of EFAC1 as it contained more micro- and mesopores. Although the surface area and the pore structure of activated carbon are crucial to accommodate the adsorbed MB, the presence of surface functional groups also played a vital role in increasing the adsorption capacity. The lower surface area EFAC2 (633 m^2/g) also allowed good adsorption capacity (q_m = 437 mg/g) and high affinity (K_L = 0.92 L/mg), possibly due to more basic surface functional groups than in the case of EFAC1, as confirmed by the wettability test. Moreover, EFAC2 contained more oxygen and hydrogen than EFAC1, as discussed in Section 3.2 (Table 3). Table 7 presents a summary of the adsorption capacities of the various adsorbents for MB. The adsorption capacities of ACFs were comparable to, or greater than some adsorbents reported in the literature.

4. Conclusion

This study reports the preparation and characterization of activated carbon foams using acid-catalyzed carbonization in polyurethane elastomer templates, followed by activation in CO_2. The objective was to provide a basis and platform synthesis process for further improvement and explore potential applications for the synthesized material such as adsorption and catalysis. The obtained ACFs have a hierarchical pore structure and exhibit a non-graphitized, turbostratic carbon nanostructure. A population of nanometre- and micrometre-sized carbon spheres are dispersed in the obtained CFs. Two activation processes were evaluated: one-step, direct activation in CO_2 and two-step activation in N_2 and CO_2. The yield of ACF was higher when direct, one-step activation was used; furthermore, direct activation at 1000 °C in CO_2 for 100 min yielded ACF with high surface area (2127 m^2/g). The temperature and time of activation played a significant role in obtaining ACF with good surface properties. Equilibrium adsorption of methylene blue (MB) was best described by the Langmuir isotherm model with a maximum adsorption capacity of 592 mg/g. One-step activation is simpler and appears more economical than two-step activation. Based on the high surface area, hierarchical pore configuration and excellent adsorption capacity of MB, the as-prepared ACFs obtained via one-step activation have the potential as an adsorbent or catalyst support. Further surface modification might enable applications in wastewater treatment.

CRediT authorship contribution statement

Mahitha Udayakumar: Conceptualization, Methodology, Validation, Visualization, Writing - original draft. **Bilal El Mrabate:** Formal analysis, Investigation, Resources. **Tamás Koós:** Investigation, Resources. **Katalin Szemmelveisz:** Investigation, Resources. **Ferenc Kristály:** Formal analysis, Investigation,

Resources, Visualization. **Máté Leskó:** Investigation, Resources, Visualization. **Ádám Filep:** Investigation, Resources, Visualization. **Róbert Géber:** Formal analysis, Investigation, Resources, Visualization. **Mateusz Schabikowski:** Formal analysis, Investigation, Resources. **Péter Baumli:** Investigation, Resources. **János Lakatos:** Investigation, Resources, Writing - original draft. **Pál Tóth:** Writing - original draft, Visualization, Project administration. **Zoltán Németh:** Writing - original draft, Supervision, Project administration, Funding acquisition.

Declaration of Competing Interest

The authors declare that they have no known competing financial interests or personal relationships that could have appeared to influence the work reported in this paper.

Appendix A. Supplementary material

Supplementary data to this article can be found online at https://doi.org/10.1016/j.arabjc.2021.103214.

References

Amini, N., Aguey-Zinsou, K.F., Guo, Z.X., 2011. Processing of strong and highly conductive carbon foams as electrode. Carbon N. Y. 49, 3857–3864. https://doi.org/10.1016/j.carbon.2011.05.022.

Amorós-Pérez, A., Cano-Casanova, L., Ouzzine, M., Rufete-Beneite, M., Romero-Anaya, A.J., Lillo-Ródenas, M.Á., Linares-Solano, Á., 2018. Spherical activated carbons with high mechanical strength directly prepared from selected spherical seeds. Materials (Basel). 11. https://doi.org/10.3390/ma11050770.

Bedin, K.C., Martins, A.C., Cazetta, A.L., Pezoti, O., Almeida, V.C., 2016. KOH-activated carbon prepared from sucrose spherical carbon: Adsorption equilibrium, kinetic and thermodynamic studies for Methylene Blue removal. Chem. Eng. J. 286, 476–484. https://doi.org/10.1016/j.cej.2015.10.099.

Bedin, K.C., Souza, I.P.A.F., Cazetta, A.L., Spessato, L., Ronix, A., Almeida, V.C., 2018. CO2-spherical activated carbon as a new adsorbent for Methylene Blue removal: Kinetic, equilibrium and thermodynamic studies. J. Mol. Liq. 269, 132–139. https://doi.org/10.1016/j.molliq.2018.08.020.

Borah, L., Goswami, M., Phukan, P., 2015. Adsorption of methylene blue and eosin yellow using porous carbon prepared from tea waste: Adsorption equilibrium, kinetics and thermodynamics study. J. Environ. Chem. Eng. 3, 1018–1028. https://doi.org/10.1016/j.jece.2015.02.013.

Brunauer, S., Emmett, P.H., Teller, E., 1938. Adsorption of Gases in Multimolecular Layers. J. Am. Chem. Soc. 60, 309–319. https://doi.org/10.1021/ja01269a023.

Bychanok, D., Plyushch, A., Piasotski, K., Paddubskaya, A., Voronovich, S., Kuzhir, P., 2015. Electromagnetic properties of polyurethane template-based carbon foams in Ka-band. Phys. Scr. 90, 094019.

Bystrzejewski, M., Lange, H., Huczko, A., Baranowski, P., Hübers, H. W., Gemming, T., Pichler, T., Büchner, B., Rümmeli, M.H., 2008. One-step catalyst-free generation of carbon nanospheres via laser-induced pyrolysis of anthracene. J. Solid State Chem. 181, 2796–2803. https://doi.org/10.1016/j.jssc.2008.07.012.

Cao, K.L.A., Rahmatika, A.M., Kitamoto, Y., Nguyen, M.T.T., Ogi, T., 2021. Controllable synthesis of spherical carbon particles transition from dense to hollow structure derived from Kraft lignin. J. Colloid Interface Sci. 589, 252–263. https://doi.org/10.1016/j.jcis.2020.12.077.

Cao, M., Feng, Y., Tian, R., Chen, Q., Chen, J., Jia, M., Yao, J., 2020. Free-standing porous carbon foam as the ultralight and flexible supercapacitor electrode. Carbon N. Y. 161, 224–230. https://doi.org/10.1016/j.carbon.2020.01.093.

Carrier, O., Bonn, D., 2015. Contact Angles and the Surface Free Energy of Solids. In: Droplet Wetting and Evaporation. Elsevier, pp. 15–23. https://doi.org/10.1016/b978-0-12-800722-8.00002-3.

Cepollaro, E.M., Caputo, D., Cimino, S., Gargiulo, N., Lisi, L., 2020. Synthesis and Characterization of Activated Carbon Foam from Polymerization of Furfuryl Alcohol Activated by Zinc and Copper Chlorides. C — J. Carbon Res. 6, 45. https://doi.org/10.3390/c6030045.

Chen, A., Li, Yuetong, Yu, Y., Li, Yunqian, Xia, K., Wang, Y., Li, S., Zhang, L., 2016. Synthesis of hollow mesoporous carbon spheres via "dissolution-capture" method for effective phenol adsorption. Carbon N. Y. 103, 157–162. https://doi.org/10.1016/j.carbon.2016.02.091.

Chen, S., He, G., Hu, H., Jin, S., Zhou, Y., He, Y., He, S., Zhao, F., Hou, H., 2013. Elastic carbon foam via direct carbonization of polymer foam for flexible electrodes and organic chemical absorption. Energy Environ. Sci. 6, 2435–2439. https://doi.org/10.1039/c3ee41436a.

Cychosz, K.A., Guillet-Nicolas, R., García-Martínez, J., Thommes, M., 2017. Recent advances in the textural characterization of hierarchically structured nanoporous materials. Chem. Soc. Rev. https://doi.org/10.1039/c6cs00391e.

de Paula, F.G.F., de Castro, M.C.M., Ortega, P.F.R., Blanco, C., Lavall, R.L., Santamaría, R., 2018. High value activated carbons from waste polystyrene foams. Microporous Mesoporous Mater. 267, 181–184. https://doi.org/10.1016/j.micromeso.2018.03.027.

Delle Site, A., 2001. Factors affecting sorption of organic compounds in natural sorbent/water systems and sorption coefficients for selected pollutants. A review. J. Phys. Chem. Ref. Data 30, 187–439. https://doi.org/10.1063/1.1347984.

Deshmukh, A.A., Mhlanga, S.D., Coville, N.J., 2010. Carbon spheres. Mater. Sci. Eng. R Reports. https://doi.org/10.1016/j.mser.2010.06.017.

Du, J., Zong, S., Zhang, Y., Hou, S., Chen, A., 2020. Co-assembly strategy for uniform and tunable hollow carbon spheres with supercapacitor application. J. Colloid Interface Sci. 565, 245–253. https://doi.org/10.1016/j.jcis.2020.01.021.

Escribano, R., Sloan, J.J., Siddique, N., Sze, N., Dudev, T., 2001. Raman spectroscopy of carbon-containing particles. Vib. Spectrosc. 26, 179–186. https://doi.org/10.1016/S0924-2031(01)00106-0.

Farhan, S., Wang, R., Jiang, H., Li, K., 2016. Use of waste rigid polyurethane for making carbon foam with fireproofing and anti-ablation properties. Mater. Des. 101, 332–339. https://doi.org/10.1016/j.matdes.2016.04.008.

Ferrari, A., Robertson, J., 2000. Interpretation of Raman spectra of disordered and amorphous carbon. Phys. Rev. B - Condens. Matter Mater. Phys. 61, 14095–14107. https://doi.org/10.1103/PhysRevB.61.14095.

Gao, N., Cheng, B., Hou, H., Zhang, R., 2018. Mesophase pitch based carbon foams as sound absorbers. Mater. Lett. 212, 243–246. https://doi.org/10.1016/j.matlet.2017.10.074.

Gilbert, P., Ryu, C., Sharifi, V., Swithenbank, J., 2009. Tar reduction in pyrolysis vapours from biomass over a hot char bed. Bioresour. Technol. 100, 6045–6051. https://doi.org/10.1016/j.biortech.2009.06.041.

Hao, E., Liu, W., Liu, S., Zhang, Y., Wang, H., Chen, S., Cheng, F., Zhao, S., Yang, H., 2017. Rich sulfur doped porous carbon materials derived from ginkgo leaves for multiple electrochemical energy storage devices. J. Mater. Chem. A 5, 2204–2214. https://doi.org/10.1039/C6TA08169J.

He, X., Wu, F., Zheng, M., 2007. The synthesis of carbon nanoballs and its electrochemical performance. Diam. Relat. Mater. 16, 311–315. https://doi.org/10.1016/j.diamond.2006.06.011.

Heidarinejad, Z., Rahmanian, O., Fazlzadeh, M., Heidari, M., 2018. Enhancement of methylene blue adsorption onto activated carbon prepared from Date Press Cake by low frequency ultrasound. J. Mol. Liq. 264, 591–599. https://doi.org/10.1016/j.molliq.2018.05.100.

Hu, J., Ren, Y., Zhang, L., 2020. Dual-confined SeS2 cathode based on polyaniline-assisted double-layered micro/mesoporous carbon spheres for advanced Li–SeS2 battery. J. Power Sources 455,. https://doi.org/10.1016/j.jpowsour.2020.227955 227955.

Huang, J., Wu, J., Dai, F., Li, C.M., 2019. 3D honeycomb-like carbon foam synthesized with biomass buckwheat flour for high-performance supercapacitor electrodes. Chem. Commun. 55, 9168–9171. https://doi.org/10.1039/c9cc03039e.

Inagaki, M., Morishita, T., Kuno, A., Kito, T., Hirano, M., Suwa, T., Kusakawa, K., 2004. Carbon foams prepared from polyimide using urethane foam template. Carbon N. Y. 42, 497–502. https://doi.org/10.1016/j.carbon.2003.12.080.

Inagaki, M., Qiu, J., Guo, Q., 2015. Carbon foam: Preparation and application. Carbon N. Y. https://doi.org/10.1016/j.carbon.2015.02.021.

Jana, P., Fierro, V., Celzard, A., 2013. Ultralow cost reticulated carbon foams from household cleaning pad wastes. Carbon N. Y. https://doi.org/10.1016/j.carbon.2013.06.020.

Jana, P., Ganesan, V., 2009. Synthesis, characterization and radionuclide (137Cs) trapping properties of a carbon foam. Carbon N. Y. 47, 3001–3009. https://doi.org/10.1016/j.carbon.2009.06.049.

Jurkiewicz, K., Pawlyta, M., Zygadło, D., Chrobak, D., Duber, S., Wrzalik, R., Ratuszna, A., Burian, A., 2018. Evolution of glassy carbon under heat treatment: Correlation structure–mechanical properties. J. Mater. Sci. 53, 3509–3523. https://doi.org/10.1007/s10853-017-1753-7.

Khalid, M., Paul, R., Honorato, A.M.B., Varela, H., 2020. Pinus nigra pine derived hierarchical carbon foam for high performance supercapacitors. J. Electroanal. Chem. 863,. https://doi.org/10.1016/j.jelechem.2020.114053 114053.

Klett, J.W., 2019. The role of precursor modification on the production of graphite foam. Carbon N. Y. 144, 43–54. https://doi.org/10.1016/j.carbon.2018.11.046.

Kumar, R., Gupta, A., Dhakate, S.R., 2015. Nanoparticles-decorated coal tar pitch-based carbon foam with enhanced electromagnetic radiation absorption capability. RSC Adv. 5, 20256–20264. https://doi.org/10.1039/c5ra00247h.

Lee, C.G., Jeon, J.W., Hwang, M.J., Ahn, K.H., Park, C., Choi, J.W., Lee, S.H., 2015. Lead and copper removal from aqueous solutions using carbon foam derived from phenol resin. Chemosphere 130, 59–65. https://doi.org/10.1016/j.chemosphere.2015.02.055.

Lee, K.T., Lytle, J.C., Ergang, N.S., Oh, S.M., Stein, A., 2005. Synthesis and Rate Performance of Monolithic Macroporous Carbon Electrodes for Lithium-Ion Secondary Batteries. Adv. Funct. Mater. 15, 547–556. https://doi.org/10.1002/adfm.200400186.

Lee, Y., Noh, S., Kim, M.S., Kong, H.J., Im, K., Kwon, O.S., Kim, S., Yoon, H., 2016. The effect of nanoparticle packing on capacitive electrode performance. Nanoscale 8, 11940–11948. https://doi.org/10.1039/c6nr02424f.

Letellier, M., Ghaffari Mosanenzadeh, S., Naguib, H., Fierro, V., Celzard, A., 2017. Acoustic properties of model cellular vitreous

carbon foams. Carbon N. Y. 119, 241–250. https://doi.org/10.1016/j.carbon.2017.04.049.

Li, L., Sun, F., Gao, J., Wang, L., Pi, X., Zhao, G., 2018. Broadening the pore size of coal-based activated carbon: Via a washing-free chem-physical activation method for high-capacity dye adsorption. RSC Adv. 8, 14488–14499. https://doi.org/10.1039/c8ra02127a.

Li, W., Liu, S., 2012. Preparation and characterization of polyurethane foam/activated carbon composite adsorbents. J. Porous Mater. 19, 567–572. https://doi.org/10.1007/s10934-011-9506-5.

Li, Y., Wang, J., Fan, S., Wang, F., Shen, Z., Duan, H., Xu, J., Huang, Y., 2020. Nitrogen-doped hierarchically porous carbon spheres for low concentration CO2 capture. J. Energy Chem. 53, 168–174. https://doi.org/10.1016/j.jechem.2020.05.019.

Li, Z., Hu, X., Xiong, D., Li, B., Wang, H., Li, Q., 2016. Facile synthesis of bicontinuous microporous/mesoporous carbon foam with ultrahigh specific surface area for supercapacitor application. Electrochim. Acta 219, 339–349. https://doi.org/10.1016/j.electacta.2016.10.028.

Liu, X., Wang, S., Sun, C., Liu, H., Stevens, L., Dwomoh, P.K., Snape, C., 2020. Synthesis of functionalized 3D microporous carbon foams for selective CO2 capture. Chem. Eng. J. 402,. https://doi.org/10.1016/j.cej.2020.125459 125459.

Marrakchi, F., Auta, M., Khanday, W.A., Hameed, B.H., 2017. High-surface-area and nitrogen-rich mesoporous carbon material from fishery waste for effective adsorption of methylene blue. Powder Technol. 321, 428–434. https://doi.org/10.1016/j.powtec.2017.08.023.

McCulloch, D.G., Prawer, S., Hoffman, A., 1994. Structural investigation of xenon-ion-beam-irradiated glassy carbon. Phys. Rev. B 50, 5905–5917. https://doi.org/10.1103/PhysRevB.50.5905.

Mestre, A.S., Pires, J., Nogueira, J.M.F., Parra, J.B., Carvalho, A.P., Ania, C.O., 2009. Waste-derived activated carbons for removal of ibuprofen from solution: Role of surface chemistry and pore structure. Bioresour. Technol. 100, 1720–1726. https://doi.org/10.1016/j.biortech.2008.09.039.

Nam, G., Choi, S., Byun, H., Rhym, Y.M., Shim, S.E., 2013. Preparation of macroporous carbon foams using a polyurethane foam template replica method without curing step. Macromol. Res. 21, 958–964. https://doi.org/10.1007/s13233-013-1114-6.

Narasimman, R., Prabhakaran, K., 2012. Preparation of low density carbon foams by foaming molten sucrose using an aluminium nitrate blowing agent. Carbon N. Y. 50, 1999–2009. https://doi.org/10.1016/j.carbon.2011.12.058.

Narasimman, R., Vijayan, S., Prabhakaran, K., 2014. Carbon foam with microporous cell wall and strut for CO2 capture. RSC Adv. 4, 578–582. https://doi.org/10.1039/c3ra46240d.

Panickar, R., Sobhan, C.B., Chakravorti, S., 2020. Chemical vapor deposition synthesis of carbon spheres: Effects of temperature and hydrogen. Vacuum 172,. https://doi.org/10.1016/j.vacuum.2019.109108 109108.

Pastore, R., Delfini, A., Micheli, D., Vricella, A., Marchetti, M., Santoni, F., Piergentili, F., 2019. Carbon foam electromagnetic mm-wave absorption in reverberation chamber. Carbon N. Y. 144, 63–71. https://doi.org/10.1016/j.carbon.2018.12.026.

Qian, X., Ren, M., Yue, D., Zhu, Y., Han, Y., Bian, Z., Zhao, Y., 2017. Mesoporous TiO2 films coated on carbon foam based on waste polyurethane for enhanced photocatalytic oxidation of VOCs. Appl. Catal. B Environ. 212, 1–6. https://doi.org/10.1016/j.apcatb.2017.04.059.

Réti, B., Kiss, G.I., Gyulavári, T., Baan, K., Magyari, K., Hernadi, K., 2017. Carbon sphere templates for TiO2 hollow structures: Preparation, characterization and photocatalytic activity. Catal. Today 284, 160–168. https://doi.org/10.1016/j.cattod.2016.11.038.

Rodríguez, E., García, R., 2017. Low-cost hierarchical micro/macro-porous carbon foams as efficient sorbents for CO2 capture. Fuel Process. Technol. 156, 235–245. https://doi.org/10.1016/j.fuproc.2016.09.002.

Saini, V.K., Pinto, M.L., Pires, J., 2013. Synthesis and adsorption properties of micro/mesoporous carbon-foams prepared from foam-shaped sacrificial templates. Mater. Chem. Phys. 138, 877–885. https://doi.org/10.1016/j.matchemphys.2012.12.077.

Shu, C., Song, B., Wei, X., Liu, Yan, Tan, Q., Chong, S., Chen, Y.Z., Yang, X.D., Yang, W.H., Liu, Y., 2018. Mesoporous 3D nitrogen-doped yolk-shelled carbon spheres for direct methanol fuel cells with polymer fiber membranes. Carbon N. Y. 129, 613–620. https://doi.org/10.1016/j.carbon.2017.12.049.

Sing, K.S.W., Everett, D.H., Haul, R.A.W., Moscou, L., Pierotti, R.A., Rouquerol, J., Siemieniewska, T., 1985. Reporting Physisorption Data for Gas/Solid Systems with Special Reference to the Determination of Surface Area and Porosity. Pure Appl. Chem. 57, 603–619. https://doi.org/10.1351/pac198557040603.

Song, Y., Zhai, G., Li, G., Shi, J., Guo, Q., Liu, L., 2004. Carbon/graphite seal materials prepared from mesocarbon microbeads. Carbon N. Y. 42, 1427–1433. https://doi.org/10.1016/j.carbon.2003.12.037.

Sze, S.K., Siddique, N., Sloan, J.J., Escribano, R., 2001. Raman spectroscopic characterization of carbonaceous aerosols. Atmos. Environ. 35, 561–568. https://doi.org/10.1016/S1352-2310(00)00325-3.

Tesfu-Zeru, T., Sakthivel, M., Drillet, J.F., 2017. Investigation of mesoporous carbon hollow spheres as catalyst support in DMFC cathode. Appl. Catal. B Environ. 204, 173–184. https://doi.org/10.1016/j.apcatb.2016.11.014.

Tondi, G., Pizzi, A., Delmotte, L., Parmentier, J., Gadiou, R., 2010. Chemical activation of tannin-furanic carbon foams. Ind. Crops Prod. 31, 327–334. https://doi.org/10.1016/j.indcrop.2009.11.013.

Torad, N.L., Hu, M., Ishihara, S., Sukegawa, H., Belik, A.A., Imura, M., Ariga, K., Sakka, Y., Yamauchi, Y., 2014. Direct synthesis of MOF-derived nanoporous carbon with magnetic Co nanoparticles toward efficient water treatment. Small 10, 2096–2107. https://doi.org/10.1002/smll.201302910.

Tsyntsarski, B., Petrova, B., Budinova, T., Petrov, N., Velasco, L.F., Parra, J.B., Ania, C.O., 2012. Porosity development during steam activation of carbon foams from chemically modified pitch. Microporous Mesoporous Mater. 154, 56–61. https://doi.org/10.1016/j.micromeso.2011.08.023.

Tuinstra, F., Koenig, J., 1970. Raman Spectrum of Graphite. J. Chem. Phys. 53, 1126–1130. https://doi.org/10.1063/1.1674108.

Udayakumar, M., El Mrabate, B., Koós, T., Szemmelveisz, K., Lakatos, J., Vanyorek, L., Németh, Z., 2019. Preparation and investigation of carbon foams from waste polyurethanes. Circ. Econ. Environ. Prot. 3, 5–15.

Ukanwa, K., Patchigolla, K., Sakrabani, R., Anthony, E., Mandavgane, S., 2019. A Review of Chemicals to Produce Activated Carbon from Agricultural Waste Biomass. Sustainability 11, 6204. https://doi.org/10.3390/su11226204.

Varila, T., Brännström, H., Kilpeläinen, P., Hellström, J., Romar, H., Nurmi, J., Lassi, U., 2020. From Norway spruce bark to carbon foams: Characterization, and applications. BioResources 15, 3651–3666. https://doi.org/10.15376/biores.15.2.3651-3666.

Varila, T., Romar, H., Lassi, U., 2019. Catalytic Effect of Transition Metals (Copper, Iron, and Nickel) on the Foaming and Properties of Sugar-Based Carbon Foams. Top. Catal. 62, 764–772. https://doi.org/10.1007/s11244-019-01171-4.

Wang, C., Shi, Z.H., Peng, L., He, W.M., Li, B.L., Li, K.Z., 2017. Preparation of carbon foam-loaded nano-TiO2 photocatalyst and its degradation on methyl orange. Surf. Interfaces 7, 116–124. https://doi.org/10.1016/j.surfin.2017.03.007.

Yadav, A., Kumar, R., Bhatia, G., Verma, G.L., 2011. Development of mesophase pitch derived high thermal conductivity graphite foam using a template method. Carbon N. Y. 49, 3622–3630. https://doi.org/10.1016/j.carbon.2011.04.065.

Yang, G.M., Xu, Q., Tian, H.W., Wang, X., Zheng, W.T., 2008. Amorphous hollow carbon spheres synthesized using radio frequency plasma-enhanced chemical vapour deposition. J. Phys. D.

Appl. Phys. 41,. https://doi.org/10.1088/0022-3727/41/19/195504 195504.

Yargic, A.S., Ozbay, N., 2019. Effect of chemical activation on the cellular structure of biopitch-derived green carbon foam. Diam. Relat. Mater. 96, 58–66. https://doi.org/10.1016/j.diamond.2019.04.032.

Yu, S., Chen, Z., Wang, Y., Luo, R., Pan, Y., 2018. A study of thermal insulation properties and microstructure of ultra-light 3D-carbon foam via direct carbonization of polymer foam. J. Porous Mater. 25, 527–536. https://doi.org/10.1007/s10934-017-0465-3.

Zhao, X., Lai, S., Liu, H., Gao, L., 2009. Preparation and characterization of activated carbon foam from phenolic resin. J. Environ. Sci. 21, S121–S123. https://doi.org/10.1016/S1001-0742(09)60053-X.

Zhao, Z., Miao, Y., Yang, Z., Wang, H., Sang, R., Fu, Y., Huang, C., Wu, Z., Zhang, M., Sun, S., Umemura, K., Yong, Q., 2018. Effects of sulfuric acid on the curing behavior and bonding performance of tannin-sucrose adhesive. Polymers (Basel). 10. https://doi.org/10.3390/polym10060651.

Zheng, M., Liu, Y., Xiao, Y., Zhu, Y., Guan, Q., Yuan, D., Zhang, J., 2009. An easy catalyst-free hydrothermal method to prepare monodisperse carbon microspheres on a large scale. J. Phys. Chem. C 113, 8455–8459. https://doi.org/10.1021/jp811356a.

Zhou, Z., Zhang, H., Zhou, Y., Qiao, H., Gurung, A., Naderi, R., Elbohy, H., Smirnova, A.L., Lu, H., Chen, S., Qiao, Q., 2017. Binder Free Hierarchical Mesoporous Carbon Foam for High Performance Lithium Ion Battery. Sci. Rep. 7, 1–9. https://doi.org/10.1038/s41598-017-01638-y.